

SIMULTANEOUS EUVE/ASCA/RXTE OBSERVATIONS OF NGC 5548

J. CHIANG¹, C. S. REYNOLDS^{1,2}, O. M. BLAES³, M. A. NOWAK¹, N. MURRAY⁴,
G. MADEJSKI⁵, H. L. MARSHALL⁶, P. MAGDZIARZ⁷

Submitted to The Astrophysical Journal, July 5, 1999

ABSTRACT

We present simultaneous observations by *EUVE*, *ASCA*, and *RXTE* of the type 1 Seyfert galaxy NGC 5548. These data indicate that variations in the EUV emission (at ~ 0.2 keV) appear to lead similar modulations in higher energy ($\gtrsim 1$ keV) X-rays by ~ 10 – 30 ks. This is contrary to popular models which attribute the correlated variability of the EUV, UV and optical emission in type 1 Seyferts to reprocessing of higher energy radiation. This behavior instead suggests that the variability of the optical through EUV emission is an important driver for the variability of the harder X-rays which are likely produced by thermal Comptonization. We also investigate the spectral characteristics of the fluorescent iron $K\alpha$ line and Compton reflection emission. In contrast to prior measurements of these spectral features, we find that the iron $K\alpha$ line has a relatively small equivalent width ($W_{K\alpha} \sim 100$ eV) and that the reflection component is consistent with a covering factor which is significantly less than unity ($\Omega/2\pi \sim 0.4$ – 0.5). Notably, although the 2–10 keV X-ray flux varies by $\sim \pm 25\%$ and the derived reflection fraction appears to be constant throughout our observations, the flux in the Fe $K\alpha$ line is also constant. This behavior is difficult to reconcile in the context of standard Compton reflection models.

Subject headings: galaxies: individual (NGC 5548) — galaxies: Seyfert — X-rays: galaxies

1. INTRODUCTION

Over the past decade, a moderately coherent picture of the broad band continuum emission from Seyfert AGNs has emerged. In this model, an accretion disk around a supermassive black hole ($M \sim 10^7$ – $10^8 M_{\odot}$) produces thermal emission primarily in the optical and ultraviolet; and a hot, Comptonizing corona above the disk up-scatters these photons to produce X-rays with energies ~ 1 – 100 keV. Furthermore, the existence of strong fluorescent iron $K\alpha$ lines at ~ 6.4 keV and the so-called “Compton reflection humps” above ~ 10 keV in the spectra of type 1 Seyferts indicate that the disk, or some other cold, optically thick material reprocesses the hard X-rays.

Central uncertainties in this model are the geometry of the corona and the disk and how the radiation from one component affects the properties and emission of the other. A cold ($T \lesssim 10^5$ K), optically thick disk will absorb a large fraction of the incident X-rays and will likely be significantly heated, thus reprocessing the absorbed energy as additional thermal photons. These photons will be available for Compton up-scattering and may provide additional cooling of the coronal electrons thereby decreasing the temperature of the Comptonizing medium. Hence, the size, shape, and location of the corona relative to the disk will affect the temperature and spectral properties of both components.

A related difficulty is the origin of the soft X-ray excess at energies $\gtrsim 0.1$ keV which has no plausible explanation within the context of standard thin disk models (Koratkar & Blaes 1999). Any reasonable range of disk temperatures for sub-Eddington accretion is too low to account for this emission as an extension of the disk thermal emission, and an extrapolation of the

standard hard X-ray thermal Comptonization spectrum down to these energies severely underpredicts the observed flux. However, Magdziarz et al. (1998) have been able to model the soft X-ray excess and most of the optical/UV as emission from very Thomson thick ($\tau \sim 30$), warm (200 eV) Comptonizing clouds above the disk. Despite the ad hoc nature of this model, it makes the definite prediction that the optical, UV and EUV flux should be highly correlated.

Correlated variability studies between different wavebands have been the traditional means of determining which spectral components provide the impetus for others. NGC 5548, in particular, has been involved in several multiwavelength monitoring campaigns, the best known of which were efforts to use optical/UV spectra to characterize the Broad Line Region via reverberation mapping (Clavel et al. 1991; Korista et al. 1995). As a by-product of these investigations, Peterson et al. (1991) compared the light curves of contemporaneous optical (4870 Å) and UV (1350 Å) data from the earlier of these campaigns and showed that essentially no lag exists between spectral bands within the temporal resolution of the observations, ± 2 days (see also Clavel et al. 1991). If the observed optical/UV flux in type 1 Seyferts is thermal emission due to the local conversion of gravitational energy in thin accretion disks, then the characteristic radii from which continuum emission at these two wavelengths are produced will be quite different. Any correlated variability between these two bands would then be limited by the sound crossing time in the disk flow. However, Courvoisier & Clavel (1991) have shown that the upper limits on the optical/UV lag for NGC 5548, as well as for Seyferts NGC 4151 and Fairall 9, are several orders of magnitude smaller than the

¹JILA, University of Colorado, Boulder CO 80309-0440

²Hubble Fellow

³Department of Physics, University of California, Santa Barbara CA 93106

⁴Canadian Institute for Theoretical Astrophysics, University of Toronto, Toronto, ON M5S 3H8, Canada

⁵Laboratory for High Energy Astrophysics, NASA/GSFC, Greenbelt MD 20771

⁶MIT Center for Space Research

⁷Deceased 1998 August

sound crossing times.

As an explanation for this near simultaneity of the optical and UV, Clavel et al. (1992; see also Malkan 1991) suggested that the variable emission is due to reprocessing of X-rays from a source located very near the central black hole. This interpretation would also be consistent with the observations of NGC 5548 by the *EUVE* satellite during the 1993 *IUE/HST*/ground-based BLR reverberation mapping campaign (Marshall et al. 1997; Korista et al. 1995). Marshall et al. obtained contemporaneous *EUVE* data and found that the EUV (at ~ 0.16 keV) also varies with the optical and UV to within $\lesssim 0.25$ days. This result links the soft X-ray excess with the lower wavebands and supports either a reprocessing model or one such as that of Magdziarz et al. (1998). In conflict with the former scenario are the contemporaneous observations of the type 1 Seyfert NGC 7469 by *RXTE* and *IUE* (Nandra et al. 1998). Over a 30 day baseline, Nandra et al. found that no simple relationship exists between the variability in the X-rays and UV. Light curves in both wavebands exhibit large, factor of ~ 2 modulations on 10 day time scales, but the peaks in the UV appear to lead the corresponding maxima in the X-rays by ~ 4 days while the troughs in the two wavebands are nearly simultaneous. Nandra et al. suggest that this behavior may be due to several reprocessing regions which interact at different time scales depending on the flux state. Previous correlated UV/hard X-ray observations of NGC 5548 by *Ginga* and *IUE* were only able to place an upper limit of ~ 6 days for the characteristic lag between these two energy bands (Clavel et al. 1992). An earlier observation by *EXOSAT* did show an apparent lag of ~ 5 ks between the soft (0.05–2.5 keV) and hard (2–10 keV) X-ray bands, but this was only seen during one of 12 observations, albeit the longest one of 60 ks, and with fairly poor statistics (Kaastra & Barr 1989; see also Nandra et al. 1991).

Another aspect of the behavior of NGC 5548 which bears upon the disk/corona geometry is the putative correlation between the derived reflection fraction and the spectral index of the underlying hard continuum (Magdziarz et al. 1998; Zdziarski, Lubiński, & Smith 1999). Spectral analyses of X-ray data from Galactic black hole candidates and Seyfert AGNs, including NGC 5548, show that the fitted reflection fraction is systematically larger for softer underlying spectra. The natural interpretation of such a correlation is that the reflecting medium is an important source of soft seed photons which affect the cooling of the Comptonizing medium. A larger covering factor implies more soft photons, causing a lower temperature coronal region and therefore a softer spectrum. Since the fluorescent iron line emission presumably also originates in this same cold, Compton reflecting material, it provides an additional diagnostic to explore the relationship between the covering factor and the spectral hardness.

In order to investigate the roles of the various components in the Seyfert disk/corona system of NGC 5548 further, we have conducted simultaneous *EUVE*, *ASCA*, and *RXTE* monitoring observations. This combination of instruments allowed us to study the soft X-ray excess, its relationship to the harder, Comptonized X-ray emission, and the higher energy signatures of X-ray reprocessing in accretion disks, the fluorescent iron $K\alpha$ line and the Compton reflection component. We describe the observations by the various instruments in § 2. In § 3, we present an analysis of the correlated variability analysis between different energy bands, and in § 4 we examine the power spectra of the various bands. In § 5, we analyze the X-ray spectral properties in detail during each observation epoch. We dis-

cuss the implications of our observations for disk/corona models in § 6 and present our summary and conclusions in § 7.

2. THE OBSERVATIONS AND DATA REDUCTION

Great effort was made to ensure that the observations by the various telescopes in this campaign were as simultaneous as possible. Unfortunately, because of differences in time allocation, conflicts with other scheduled observations, differing visibility constraints and other unforeseen complications, absolute simultaneity over our proposed 23 day baseline was not possible. In particular, several data gaps of a few $\times 10$ ks exist in the *RXTE* data because of scheduling conflicts; the *EUVE* spacecraft went into “safepoint” mode just prior to one of our shorter monitoring observations; and the final *RXTE* observation which took place over a 200ks time period had no contemporaneous *EUVE* or *ASCA* monitoring because of visibility constraints. Nonetheless, these data represent some of the highest time resolution broad band monitoring of any AGN.

In order to provide uniformity in referring to the various pointings performed by the three satellites, we have adopted a numbering scheme based on the originally scheduled simultaneous observations. In this scheme, the June 15, June 18–24, July 1 and July 7 observations are numbered 1–4, with the June 18–23 (obs. 2) subdivided as we discuss below. We refer to all the other observations taken by individual instruments by the dates on which they took place.

2.1. EUVE

Our strategy for using *EUVE* to monitor the soft X-ray flux from NGC 5548 was identical to that employed by Marshall et al. (1997). Photometry was carried out using the Deep Survey (DS) detector with the Lex/B filter, and the pointing was offset from nominal by 0.3 degrees along the direction of the SW spectrometer dispersion axis. This was done in order to avoid the deadspot in the DS detector while largely preserving the capabilities of the SW spectrometer. In extracting the count rates, we employed the analysis of Marshall et al. which accounts for dead-time and “Primbsch” corrections as in the standard *EUVE* analysis procedure and which also applies a vignetting correction necessitated by the offset pointing. Another important feature of this analysis is its implementation of a maximum likelihood technique using the instrumental point spread function to determine the source and background counts rather than specifying source and background apertures. Further information on these procedures can be found in Marshall et al. (1997).

Table 1 gives the details of our *EUVE*-DS observations. The spectral densities we report account for a Galactic column density of $N_H \simeq 1.7 \times 10^{20} \text{ cm}^{-2}$ and assume a power-law spectrum with index 0–2 ($f_\nu \propto \nu^{-\alpha}$). For the narrow effective bandpass we consider (70–90Å), the resulting spectral densities we compute are not very dependent on the value of α . The 1998 June 2, June 9, and July 1 observations were simultaneous with Lick observations scheduled on those dates, although the June 2 Lick observation did not occur due to bad weather. As we noted earlier, the *EUVE* spacecraft went into “safepoint” mode just prior to our June 15 joint *ASCA/RXTE* observations (cf. Tables 2 & 3), and we did not obtain simultaneous *EUVE* data for our July 7 *ASCA/RXTE* observations because of a scheduling error.

2.2. ASCA

2.2.1. Basic data reduction

ASCA observed NGC 5548 on five occasions during this campaign. The dates, good exposure times, count rates and 2–10 keV fluxes are reported in Table 2. *ASCA* possesses four detectors; two solid-state imaging spectrometers (SIS0 and SIS1) and two gas-imaging spectrometers (GIS2 and GIS3). These detectors are located at the focal points of four independent but coaligned X-ray telescopes. During our campaign, data from all four detectors were obtained. SIS data taken in both BRIGHT and FAINT mode were combined in order to maximize the total signal and a standard GRADE selection was performed in order to reduce the effects of particle and instrumental background. Data from the SIS were further cleaned in order to remove the effects of hot and flickering pixels and subjected to the following data-selection criteria: the satellite should not be in the South Atlantic Anomaly (SAA), the object should be at least 5° above the Earth’s limb, the object should be at least 25° above the day-time Earth limb, and the local geomagnetic cut-off rigidity (COR) should be greater than 6 GeV/c. Data from the GIS were cleaned to remove the particle background and subjected to the following data-selection criteria: the satellite should not be in the SAA, the object should be at least 7° above the Earth’s limb and the COR should be greater than 7 GeV/c. These steps were performed using XSELECT v1.4 which is part of the FTOOLS v4.1 package.

Images, light curves and spectra were extracted from the good data using a circular region centered on the source. For the SIS, an extraction radius of 3 arcmins is used whereas a radius of 4 arcmins is used for the GIS. These regions are sufficiently large to contain all but a negligible portion of the source counts. Background spectra were extracted from source free regions of the same field of view within each of the four *ASCA* instruments. Background regions for the SIS were taken to be rectangular regions along the edges of the source chip whereas annular regions were used to extract GIS background. Approximately 1% of the photons in the source extraction region were found to be from the background.

2.2.2. The effects of RDD

The effects of radiation damage to the CCD’s of both SIS detectors have reduced the ability of the on-board software to estimate and correct for dark current. This problem is known as residual dark distribution (RDD) and, in these late stages of the *ASCA* mission, is becoming a major concern. Data taken in FAINT mode can have the effects of RDD partially corrected for during the ground-based reduction process. Unfortunately, due to telemetry constraints, the majority of our data were taken in BRIGHT mode and cannot be corrected.

Operationally, RDD renders the soft end of the SIS spectrum (< 1 keV) untrustworthy. Comparing our SIS0 and SIS1 spectra reveals major discrepancies between these two instruments below 1 keV which are readily attributed to RDD effects. For this reason, we restrict ourselves to the 2–10 keV band when performing spectral fitting with SIS data.

2.2.3. An SIS/GIS discrepancy

The spectral fitting described below was initially performed using the 2–10 keV data from all four *ASCA* instruments. However, the GIS spectra were found to strongly disagree with the SIS spectra at high-energies (8–10 keV) — the two GIS spectra consistently lay above the two SIS spectra in each and every observation of this campaign. When these spectra are fitted with a spectral model consisting of an absorbed power-law model and a Gaussian emission line (see below), residuals are present in

the GIS spectra at energies coincident with the Gold M-edge (2.2 keV) and Xenon L-edge (4.8 keV). This strongly indicates the use of an incorrect GIS gain factor. No linear gain correction could eliminate these residuals simultaneously. Faced with the conclusion that there is a non-linear gain problem in our GIS data, we choose not to use GIS data in any of the spectral fitting reported below.

Further support for the hypothesis that the GIS is in error is given when *RXTE*-PCA data are fitted simultaneously with these *ASCA* data. In the overlap band (4–10 keV), the PCA spectra generally agree well with SIS spectra and disagree with GIS spectra. However, to our knowledge, the *ASCA* and *RXTE* instruments have not been cross-calibrated. As we discuss below, we have therefore allowed the relative normalization for the spectral models which are fit to data from each instrument to vary, and we have also allowed the spectral index of the hard continuum to vary separately for the SIS and PCA data.

2.3. RXTE

Standard extraction methods were employed to determine the PCA and HEXTE light curves and spectra. The PCA instrument consists of five collimated (1° FWHM) proportional counter units (PCUs) which are numbered 0–4. Each PCU contains three multianode detector layers with a mixture of xenon and methane gas, has a bandpass of 2–60 keV and a geometric collecting area of $\sim 1400\text{cm}^2$. The energy resolution of each detector is $\sim 8\%$ FWHM at 6.6 keV (Glasser, Odell, & Seufert 1994). PCA data were collected only from PCUs 0–2, since PCUs 3 and 4 were turned on for a smaller fraction of the on-source time due to breakdown. This source is relatively weak, so in order to maximize signal-to-noise, we accumulated events only from the top xenon/methane layer of the PCA. As recommended by the PCA team, data were discarded for the 30 minutes following a SAA passage, during Earth occultation (i.e., when the Earth elevation angle is $< 10^\circ$), and when there is severe electron contamination. The variability and spectral analyses were greatly facilitated by the recently developed faint source ($\lesssim 40$ cps) background model. It is implemented in the PCABACKEST program and is contained in the model files `pca_bkgd_faint17_e03v03.mdl` and `pca_bkgd_faint240_e03v03.mdl`. The first file contains information on the variation on the “L7” rate which is a background rate made up of a combination of 7 rates in pairs of adjacent signal anodes, while the second file is related to the integrated recent particle doses during SAA passages, as measured by the HEXTE particle monitor. SAA passages and doses are recorded in `pca_saa_history_v8`. Response matrices were constructed using PCARMF v3.5 and PCARSP v2.36. For spectral fitting, we restricted the energy range of the PCA data from 3 to 20 keV.

The HEXTE instrument consists of two clusters of four NaI/CsI-phoswich scintillation counters which are sensitive from 15 to 250 keV with an open area of $\sim 900\text{cm}^2$ for each cluster. Beam switching or “rocking” of these clusters between source and background fields provided direct measurements of the HEXTE background with an on-source duty cycle of $\sim 60\%$. As recommended by the HEXTE team, data were discarded for the 2 minutes following a SAA passage and during Earth occultation. Standard deadtime corrections were applied to the Science Archive data. In order to maximize signal-to-noise in the light curves, only counts from absolute detector channels 30–122 were used. As can be seen from Table 3,

the HEXTE count rates were very low, $\lesssim 1$ cps throughout our observations. Hence, statistically meaningful HEXTE spectra could only be accumulated over relatively long integrations, $\gtrsim 4 \times 10^5$ s, which is substantially longer than the variability time scale seen in the PCA data.

2.3.1. 1E 1415.6+2557

A minor complication in the *RXTE* analysis is the existence of a contaminating source within the field-of-view of the PCA and HEXTE collimators, 0.5° away from NGC 5548. The source is a BL Lac object, 1E 1415.6+2557, and has been previously observed by *ROSAT* (Nandra et al. 1993). As an additional precaution, since Nandra et al. reported several additional sources in the *ROSAT*-PSPC FOV surrounding NGC 5548, we performed a PCA scanning observation of the field to determine if any other contaminants were present (cf. Marshall et al. 1998). Using the collimator response model of the PCA which was provided to us by the PCA instrument team, we fit the scan observations and found that we could account for all the counts in the field adequately with just two sources: NGC 5548 and 1E 1415.6+2557.

During the first four of our *RXTE* observing periods, the contribution by 1E 1415.6+2557 to our NGC 5548 measurements was determined from ~ 3 –5 ks pointings directed at 1E 1415.6+2557 just prior to and after each NGC 5548 observation period. This bracketing was done in case 1E 1415.6+2557 exhibited any variability on 30 ks time scales. We used the aforementioned collimator model to fit the count rates from these two sources simultaneously during the beginning and ending sub-portions of each observation. We then extracted spectra from these sub-portions for each source. The spectra for 1E 1415.6+2557 were fit with XSPEC v10.00 using the associated background-subtracted NGC 5548 spectrum as a “correction file”, appropriately scaled to yield the fitted count rates. Table 5 gives the estimated count rates and spectral fits for 1E 1415.6+2557 obtained from this procedure. When there are significant differences in the count rates of 1E 1415.6+2557 for the two bracketing pointings, they are reported separately, i.e., as 2a/b and 3a/b.

For the observations beginning 1998 August 16, we altered our strategy for estimating the flux and spectrum from 1E 1415.6+2557. Rather than relying on scaled spectral correction files extracted from direct pointings at NGC 5548 which are in turn contaminated by flux from 1E 1415.6+2557, we took “background” measurements at the symmetric location on the opposite side of NGC 5548. For the same roll angles, these pointings should contain the same contribution from NGC 5548 as the direct 1E 1415.6+2557 pointings, but since they are $\sim 1^\circ$ away, they should be uncontaminated by 1E 1415.6+2557 itself. Correction files from these pointings were then used in the spectral analysis. We find that the spectrum of 1E 1415.6+2557 during the August 16 observations was somewhat harder and the count rate in the PCA had increased by $\sim 40\%$. We note that this increase is not due to our altered observing strategy as we have also applied the collimator model fitting method and confirm this result. The collimator response for pointings directed at NGC 5548 to photons from 1E 1415.6+2557 is ~ 0.33 , so the contaminating contribution to the NGC 5548 light curves will be ~ 2 cps with a modulation of $\lesssim 0.8$ cps, while the PCA count rates for NGC 5548 are typically 20–25 cps. Therefore, in our variability analysis of NGC 5548, we can safely ignore contributions from 1E 1415.6+2557.

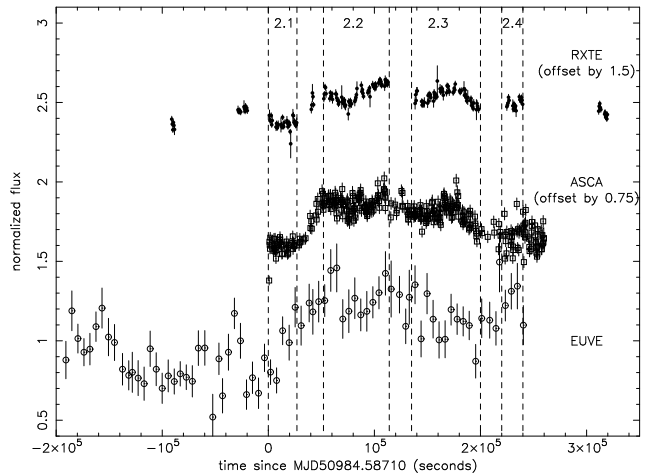


FIG. 1.— *EUVE*, *ASCA*-SIS, and *RXTE*-PCA light curves for the long observation. All light curves have been normalized to unity mean. For clarity, the *ASCA* and *RXTE* curves were then offset by 0.75 and 1.5 respectively. The dashed lines show the boundaries of the four intervals which were used for studying the intra-observation spectral variability.

3. CORRELATED VARIABILITY

In Fig. 1, we show the *EUVE*, *ASCA*, and *RXTE*-PCA count rate light curves for the longest of our contemporaneous observation periods. The most distinct feature in all three of these light curves is the large step at $\sim 2 \times 10^4$ s in the figure. This step is more pronounced ($\sim 40\%$) at EUV energies than in the harder X-rays ($\sim 20\%$ for the *RXTE*-PCA data). After this step, in the *RXTE* light curve there are several local maxima which recur on ~ 50 ks time scales; similar modulations also appear in the *EUVE* light curve, but with less certainty due to the relatively poor statistics. As a first order analysis of the spectral variability across these wavebands, we have computed cross-correlation functions (CCFs) for each pair-wise combination.

The method we use is the Z-transformed Discrete Cross-Correlation Function (ZDCF) of Alexander (1997) based upon the DCF method of Edelson & Krolik (1988). In the latter procedure, which was designed to accommodate unevenly and differently sampled data trains, pair-wise combinations of measured flux values from the two light curves are binned according to their relative delays or lags. For the data pairs within each lag bin, a quantity which is essentially Pearson’s linear correlation coefficient is computed (Press et al. 1992). In the continuum limit, this procedure is equivalent to the standard definition of the CCF. Alexander (1997) proposed two modifications of this method: first, the lag bins are defined to contain a specific number of data pairs which should be > 11 in order to ensure convergence; second, the errors are estimated by applying the Z-transform to the correlation function values and using the number of pairs for the given bin and known properties of the Z-transform to estimate the errors. For identical binning, the ZDCF estimates of the CCF are equal to those produced by the DCF, but the uncertainties are better behaved. Auto-correlation functions can also be computed by this method.

Figure 2 shows the ZDCFs for *EUVE* vs 0.5–1 keV *ASCA*-SIS, *EUVE* vs *RXTE*-PCA, and 0.5–1 keV *ASCA*-SIS vs *RXTE*-PCA. In each case, a positive time delay indicates the latter light curve lagging the former. In order to obtain a quantitative estimate of the relative lags, we fit the ZDCF values in the vicinity of the peak with a parabola (solid curves in Fig. 2). This functional form has no specific physical meaning—it is merely a

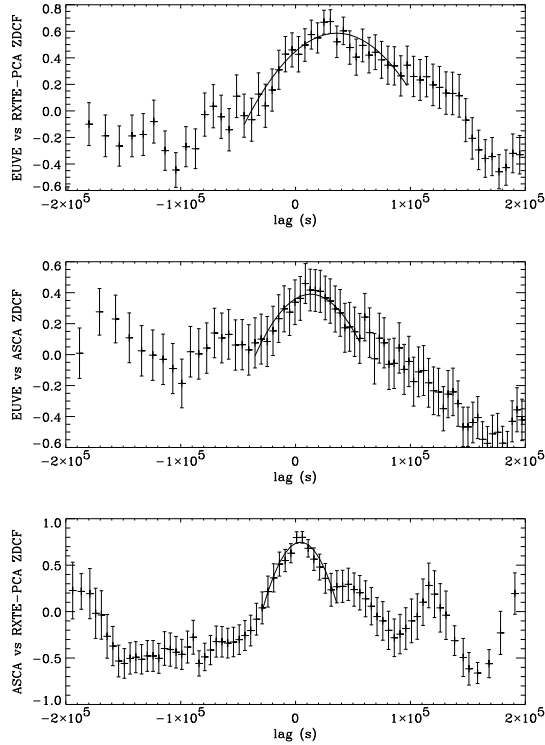


FIG. 2.— Cross-correlation functions computed using the ZDCF (Alexander 1997). The bands which are compared are *EUVE* (0.14–0.18 keV), *ASCA* (0.5–1 keV), and *RXTE-PCA* (2–20 keV) (cf. Fig. 1). The solid curves are the parabolas which were fit to find the location of the characteristic lags.

convenient parametrization of the ZDCF shape near the maximum. From these fits, we see that higher energy light curve modulations are delayed relative to lower energy ones with the variations in the 2–20 keV *RXTE-PCA* data lagging those of the *EUVE* by ~ 35 ks and those of the 0.5–1 keV *ASCA* data by ~ 5 ks. Similarly, the 0.5–1 keV *ASCA* data lag the *EUVE* by ~ 13 ks. We determine confidence limits using Monte Carlo methods where for each trial we produce simulated light curves taking the measured light curves as input and assuming Gaussian statistics. In Table 4, we report the mean value of the fitted peaks and the 99.9% C.L.s for each pair of light curves. We have also estimated the cross-correlation function using the Lomb-Scargle method for computing the FFT of unevenly sampled data (Scargle 1989) and find essentially the same results.

4. POWER SPECTRA

We can combine our pointed X-ray observations, which span time scales from approximately 5×10^3 s to 3×10^5 s, with observations from the All Sky Monitor (ASM) on board the *RXTE* spacecraft, which span time scales ranging from days to 3 years. We have used these data to construct an X-ray power spectrum that covers four orders of magnitude in Fourier frequency from 10^{-8} – 10^{-4} Hz. The result is presented in Fig. 3. A power spectrum that covers a similarly broad range of time scales, but with much better statistics, has been obtained from pointed *RXTE* observations of the Seyfert 1 galaxy NGC 3516 (Edelson & Nandra 1999).

As the orbital time scales of the *RXTE*, *ASCA*, and *EUVE* spacecraft are approximately 5 ks, significant variability power (due to SAA passages and source occultation) appears on these time scales and at higher harmonics. In addition, for the *EUVE*

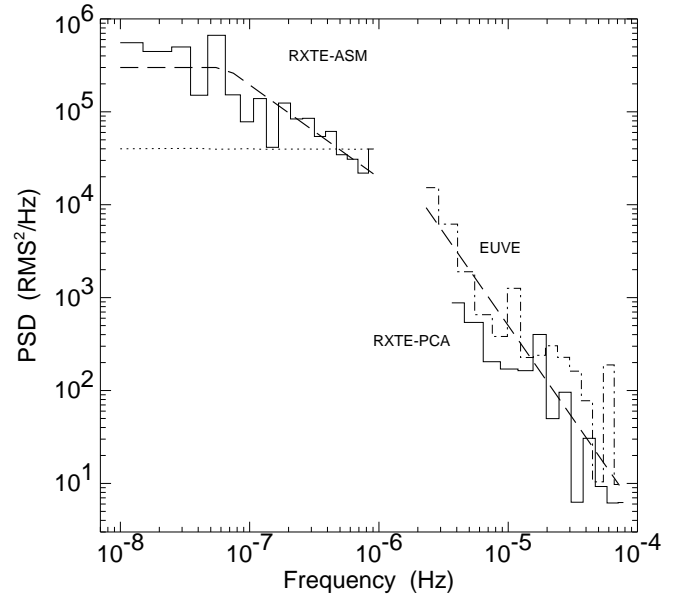


FIG. 3.— Power Spectral Densities constructed from *RXTE-ASM*, *RXTE-PCA*, and *EUVE* data (see text). Dashed lines show flat, f^{-1} , and f^{-2} overlaid on the power spectra. The dotted line shows our estimate of the mean noise level of the ASM data. All PSDs are normalized such that integrating over positive Fourier frequencies yields the root mean square variability, normalized to the mean, for each particular light curve.

spacecraft, we must integrate for approximately 5 ks in order to obtain good signal to noise. We therefore only consider Fourier frequencies $< 10^{-4}$ Hz. The PSDs are constructed from light curves with 5.6 ks time bins for the *EUVE* data, and 128 s time bins for the *RXTE-PCA* data. These light curves, however, still contain a number of data gaps, therefore we use techniques for calculating power spectra of unevenly sampled light curves (see Lomb 1976; Scargle 1982). The PSDs are then normalized so that integrating over positive frequencies yields the root mean square (rms) variability relative to the mean (see Belloni & Hasinger 1990a; Miyamoto et al. 1992). The resulting PSDs are then logarithmically binned over frequencies ranging from $f \rightarrow 1.2f$. For the *EUVE* PSD we calculate that the noise contribution to the rms variability is $11.0 \pm 0.6\%$ of the mean, therefore we subtract this (assumed white) noise level from the *EUVE* PSD. The noise level of the *RXTE* PSD is negligible.

Several results are immediately apparent in Fig. 3. First, we see that the *EUVE* light curve is more highly variable than the *RXTE-PCA* light curve, with an rms variability of $18.1 \pm 1.4\%$ compared to $7.4 \pm 0.6\%$ over the time scales sampled by the PSDs. Both the *RXTE-PCA* and the *EUVE* PSDs are approximately $\propto f^{-2}$. The f^{-2} PSD seen for the *RXTE-PCA* light curve is comparable, in both shape and rms amplitude, to the high-frequency (> 3 Hz) PSDs seen for galactic black hole candidates (GBHCs), such as Cygnus X-1, observed in their low/hard states (Miyamoto et al. 1992; Nowak et al. 1999a).

The low-frequency X-ray PSD is calculated via ASM data. The ASM provides light curves in three energy bands, 1.3–3.0 keV, 3.0–5.0 keV, and 5.0–12.2 keV, typically consisting of several 90 s measurements per day (see Levine et al. 1996; Remillard & Levine 1997; Lochner & Remillard 1997). We have combined all three energy channels into a single channel, and then rebinned the data on 5 day time scales. Here we have filled data gaps (39 out of 233 points) with a linear interpolation, and the power spectrum is then constructed using standard

FFT techniques. We did not subtract the expected noise level calculated from the ASM error bars, as the derived PSD does not flatten at this level. This indicates that either the ASM error bars are overestimated or that they do not follow gaussian statistics.

The derived PSD is approximately flat at low frequencies, shows a possible break at $\approx 7 \times 10^{-7}$ Hz (≈ 200 day period), and is consistent with an f^{-1} dependence at higher frequencies. The extent to which the PSD remains flat at low frequencies is uncertain due to the limited time-span of the ASM observations compared to the putative 200 day break period. We note that Czerny, Schwarzenberg-Czerny, & Loska (1999) find a break in the optical power spectrum at a period $\lesssim 1000$ days. The slope of the ASM-PSD at high frequencies is also uncertain due to the large noise level (shown as a dotted line in Fig. 3). The rms amplitude of the ASM lightcurve, including noise, is $\approx 30\%$. A Lomb-Scargle periodogram yields comparable results, and also shows a formally significant (via the methods of Horne & Bailunas 1986) peak at a 200 day period. This peak is coincident with the break in the PSD, and furthermore the methods of Horne & Bailunas are only strictly valid for a single sinusoidal period buried within pure counting noise.

The overall X-ray PSD is again remarkably similar in both shape and rms amplitude to those seen in the low/hard states of GBHCs. Low state GBHCs such as GX 339–4 (Nowak et al. 1999b) or Cyg X-1 (Belloni & Hasinger 1990a; Miyamoto et al. 1992; Nowak et al. 1999a) typically have an rms amplitude of 30–40%, a flat PSD at low frequency with a break into an f^{-1} spectrum at 0.03–0.3 Hz, and a further break into an f^{-2} spectrum at 1–10 Hz. The X-ray PSD we have found for NGC 5548 is comparable to this, except scaled to approximately a factor of 10^6 lower in frequency (although we do not resolve the break into the f^{-2} spectrum). A similar result was found for the X-ray PSD of NGC 3516 (Edelson & Nandra 1999).

The factor of 10^6 is comparable to the expected ratio of the black hole masses between these two kinds of systems. Furthermore, the 10^4 s time delays between the ASCA and hard RXTE bands discussed above are scaled by a similar factor compared to the 10^{-3} – 10^{-2} s X-ray time lags seen at the 1–10 Hz break frequency in the low/hard state of GBHCs (see Miyamoto & Kitamoto 1989; Nowak et al. 1999a). In the high-frequency regime in GBHCs, the variability coherence between X-ray bands begins to break down (Vaughan & Nowak 1997; Nowak et al. 1999a; Nowak et al. 1999b). In these regimes, we therefore do not expect a perfect linear correlation between energy bands. Carrying the analogy to GBHCs further, low/hard state GBHCs exhibit X-ray time lags of 0.03–0.1 s at the lower break frequency (Miyamoto & Kitamoto 1989; Nowak et al. 1999a; Nowak et al. 1999b), hence one might expect $\mathcal{O}(10^5)$ s time delays in the observed $\mathcal{O}(100)$ day time scale variability. This is likely below the detection threshold of the RXTE-ASM, and we find no evidence for such delays comparing the lowest and highest ASM channels. Such time delays, however, if they were to exist, will likely be detectable by future all sky monitors with larger effective area and somewhat longer sampling time scales.

5. X-RAY SPECTRAL FITTING

In this section we use standard spectral fitting techniques to characterize the X-ray energy spectrum of NGC 5548. From previous X-ray studies, we expect the spectrum to be dominated

by non-thermal power-law continuum emission. In addition, a relativistically broad iron emission line (from the surface of the accretion disk) and an associated reflection continuum will be superposed on this power-law continuum. These expectations guide our choice of spectral models (described below), and are confirmed in the sense that our spectral models describe the data very well. As we noted previously, we restrict our attention to data above 2 keV because of RDD effects; this removes the necessity to model the warm absorber in this object. All spectral fitting has been performed using XSPEC v10.00.

In order to search for spectral variability, we examined X-ray spectra from ten distinct time intervals. For seven of these intervals, we have simultaneous ASCA/RXTE data: observations 1, 3 and 4, as well as four sub-intervals of observation 2 (defined in Fig. 1). The three additional intervals for which only RXTE observed occurred just prior to and after observation 3 and during the period 16–18 August 1998 (cf. Tables 3 and 6). This set of spectra allows us to probe both long (weekly) and short (daily) time scale spectral variability. The overlapping ASCA and RXTE data were pruned in order to ensure strict simultaneity of the spectra from the two instruments. This was necessary since the observations for both satellites were interrupted either due to scheduling conflicts (RXTE) or telemetry failures (ASCA). However, since we are not examining spectra from data which are integrated over intervals of less than several tens of ks, we have neglected non-simultaneity on shorter time scales such as the orbital period.

Since the count rates obtained from the RXTE-PCA observations are much greater than that of the ASCA-SIS, we consider the RXTE-PCA data by itself initially. We then use those fits to guide our joint SIS/PCA fits, relying upon the greater spectral resolution of the ASCA detectors to constrain the iron line component better.

5.1. The RXTE data

We fit several models to these data. Our initial model is a simple power-law modified by Galactic neutral absorption ($N_{\text{H}} = 1.7 \times 10^{20}$ cm $^{-2}$; $z = 0$).¹ This proves to be an unacceptable fit in all ten cases, with residuals clearly indicating the need for an iron emission line and spectral hardening above 10 keV. Next, we add a narrow emission line to the power-law spectrum with a (rest-frame) energy fixed to that of the $K\alpha$ line of cold iron (6.4 keV). Using the F-test, this leads to a significant improvement (at greater than the 99% level) in the goodness-of-fit in all of the datasets. Adding more complexity to the fit, the iron line is allowed to have a broad Gaussian profile and arbitrary energy. Again using the F-test, this leads to a significant improvement (at the 90% level) in the goodness-of-fit in two cases only (observations 1 and 2.2).

Proceeding to more physical models, we replace the Gaussian emission line profile with the iron line profile expected from a relativistic accretion disk around a Schwarzschild black hole (Fabian et al. 1989). The inner edge of the line emitting region, the inclination of the disk, and the normalization of the line are free parameters in this fit. Hidden fixed parameters are the outer edge of the line emitting region, r_{out} , the line emissivity index β defined such that the local line emissivity is proportional to $r^{-\beta}$, and the rest frame line energy which is fixed at 6.4 keV. The emissivity index β is fixed at

¹For all the fits to the RXTE-PCA data, we include a fixed power-law to represent the contamination by 1E 1415.6+2557. The spectral indices used for this added power-law are shown in Table 5. The flux normalizations at 1 keV shown in that table are reduced by a factor determined by the collimator response to 1E 1415.6+2557 for each pointing directed at NGC 5548. This factor is typically ~ 0.33 .

$\beta = 2.5$ which approximates the expected emissivity in a variety of physical scenarios. The outer radius r_{out} is fixed at $1000r_g$, where $r_g = GM/c^2$ is the gravitational radius of the central black hole. For our chosen value of β , the fits are insensitive to the value of r_{out} , provided that $r_{\text{out}} > 100r_g$. Although this is a more physical model, the *RXTE*-PCA data cannot distinguish it from the Gaussian line profile, i.e., there is no improvement in the goodness-of-fit in any of the datasets when the diskline profile is used. We do note, however, that both the broad Gaussian and the diskline fits are consistent with a substantial fraction of the iron emission originating from within $\sim 20r_g$.

Our final models include the Compton reflection continuum which is implemented in XSPEC as the PEXRAV model (Magdziarz & Zdziarski 1995). We fix the e -folding energy of the underlying hard continuum at 120 keV as determined from fits by Magdziarz et al. (1998) to data from *OSSE* observations of NGC 5548, and we set the inclination of the planar cold reflector at 30° . We also fix the chemical abundances to be Solar. The relative normalization of this component, \mathcal{R} , is left as a free parameter. For an isotropic primary X-ray source, $\mathcal{R} = \Omega/2\pi$, where Ω is the solid angle subtended by the cold reflecting medium as seen by an observer situated at the X-ray source. This leads to a large improvement in the goodness-of-fit for all of the observations, showing that the Compton continuum (which produces the high-energy spectral hardening) is clearly detected.

5.2. Joint ASCA/RXTE spectral fitting

Four of our *ASCA* observations were scheduled to be contemporaneous with *RXTE* observations. Joint spectral fitting of simultaneous data from *ASCA*-SIS and *RXTE*-PCA can be a powerful technique — it allows us to utilize both the spectral resolution of *ASCA* and the broad-band sensitivity of *RXTE*. The results of the joint *ASCA*-SIS/*RXTE*-PCA fits for our seven intervals are listed in Table 6. To facilitate direct comparison, we show the fits to the *RXTE*-PCA data alone which include a broad Gaussian emission line. The addition of the *ASCA* data does not affect the model fits greatly, although in some cases it allows the iron line width to be resolved.

5.3. Observed correlations between spectral parameters

Here we use the results of our spectral fitting of the *ASCA* and *RXTE* data to examine spectral variability. In order to ensure that we have a set spectral parameters which have been uniformly analyzed, we consider only those parameters which have been obtained from fits to the *RXTE* data alone. Spectral parameters from the joint *ASCA*/*RXTE* fits yield similar results. Figure 4 shows the photon index Γ , the iron line flux N_l , the iron line equivalent width $W_{K\alpha}$, and relative reflection normalization \mathcal{R} as a function of the 2–10 keV flux, F_{2-10} , of the hard continuum component. For these plots and all of the fits to the spectral trends discussed in this section, we present uncertainties as $1-\sigma$ error bars.

5.3.1. The photon index

There is a clear positive correlation between the photon index and the 2–10 keV flux (Fig. 4a). Fitting a simple linear form to this correlation gives

$$\Gamma = (1.63 \pm 0.04) + (0.030 \pm 0.006) \left(\frac{F_{2-10}}{10^{-11} \text{ erg s}^{-1} \text{ cm}^{-2}} \right). \quad (1)$$

This simple model does not strictly provide a formally adequate description of the spectral variation with flux, giving a

goodness-of-fit of $\chi^2/\text{dof} = 16.1/8$. However, we note that most of the contribution to this large value of χ^2 is due to the Aug 16–18 data point. Omitting this point, we find $\chi^2/\text{dof} = 5.7/7$ with the fit parameters being substantially unchanged. Nonetheless, the fact that the X-ray continuum gets softer when brighter is consistent with the trend observed in previous monitoring campaigns of this source (Magdziarz et al. 1998). However, here we appear to find a somewhat weaker dependence of spectral index on flux.

5.3.2. Iron line and reflection features

Correlations of the iron line strength with the continuum flux are of great importance. In the simple X-ray reflection scenario, we would expect $W_{K\alpha}$ to be constant provided that the light crossing time of the fluorescing region is much smaller than the time scale on which spectral variability is being probed. If the light crossing time of the emission line region is much greater than the time scale being probed, a constant iron line flux, N_l , would be expected. When these two time scales are comparable, reverberation effects come into play and both N_l and $W_{K\alpha}$ will be seen to vary.

Like $W_{K\alpha}$, the parameter \mathcal{R} should measure the amount of X-ray reflection relative to the direct continuum. Indeed, $W_{K\alpha}$ should be proportional to \mathcal{R} provided the following conditions are satisfied:

1. The Compton reflection continuum is not starting to dominate the observed continuum at the iron line energies. In practice, this condition implies $\mathcal{R} < 2-3$.
2. The ionization state of the illuminated regions of the reflecting medium is fixed.
3. The primary continuum has a fixed energy spectrum. Of course, we have just shown that this is not strictly the case and that the photon index of the primary continuum emission changes by $\Delta\Gamma \sim 0.2$ during our campaign in a manner that is well correlated with the 2–10 keV flux. However, the Monte Carlo simulations of George & Fabian (1991) show that such small photon index changes only have a small (less than 10%) effect on the iron line equivalent width.

Apart from inclination dependences (which are usually weak) and ionization gradients, the geometry of either the reflecting medium or the X-ray source does not affect the expected proportionality of \mathcal{R} and $W_{K\alpha}$.

Our spectral results hint at a more complex picture. Inspection of Fig. 4b shows that the iron line flux is essentially constant. This is borne out by the linear (dotted line) and constant (solid) models which we have fit and which describe these data very well. Apart from effects introduced by the subtle changes in photon index, this implies that $W_{K\alpha}$ is inversely proportional to the flux (Fig. 4c). More formally, fitting the 10 data points in the $W_{K\alpha}$ - F_{2-10} plot with a constant model results in $\chi^2/\text{dof} = 20.8/9$ (dotted curve), unacceptable at the 97% level. Assuming, instead, a power-law relationship between these two parameters such that $W_{K\alpha} \propto F_{2-10}^\alpha$ results in a dramatic improvement in the goodness-of-fit with $\chi^2/\text{dof} = 7.9/8$ and $\alpha = -0.9 \pm 0.4$ (solid curve in Fig. 4c). Thus, these results are consistent with a constant line flux and an equivalent width which is inversely proportional to the continuum flux.

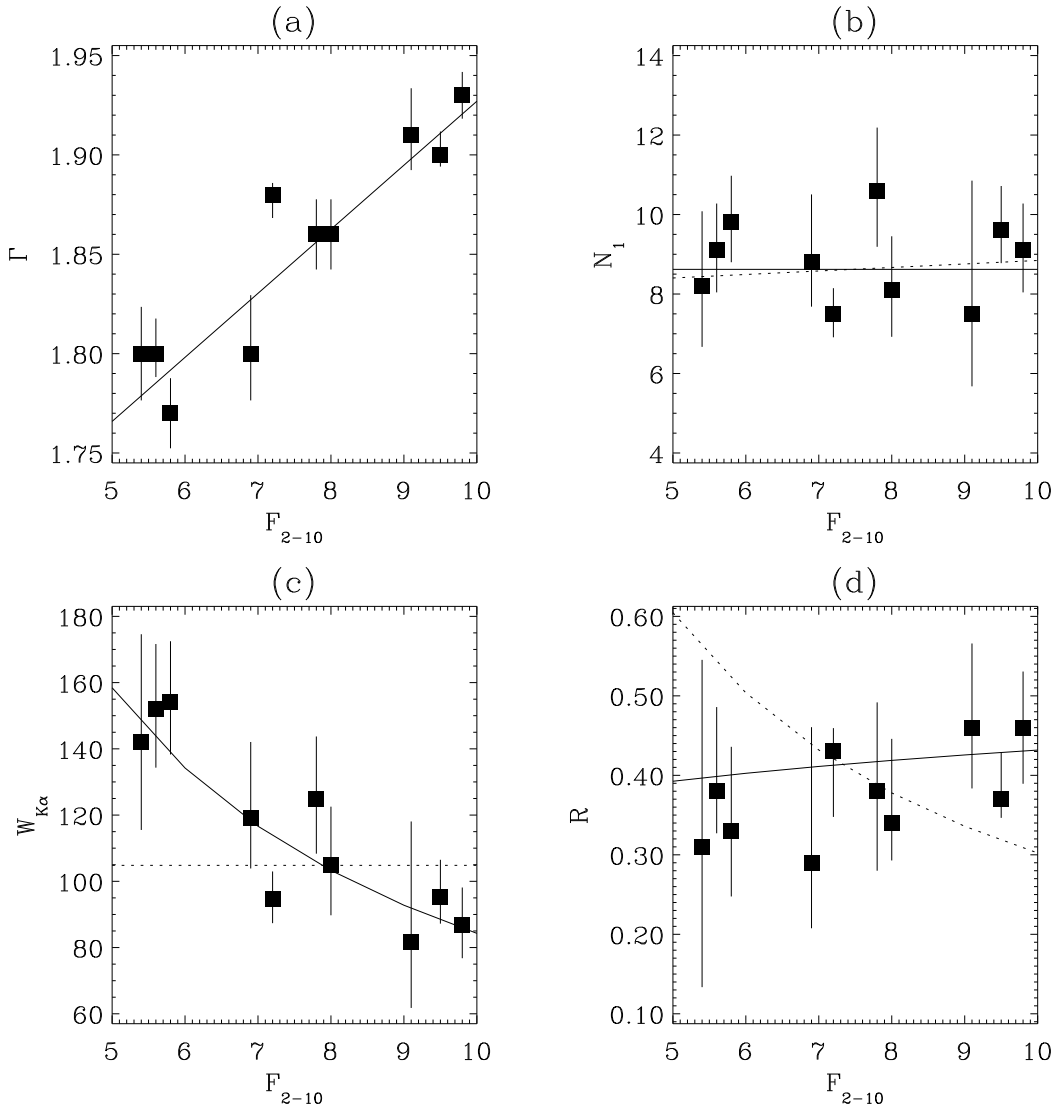


FIG. 4.— (a) Photon index Γ , (b) iron line flux N_1 , (c) iron line equivalent width $W_{K\alpha}$, and (d) relative reflection normalization \mathcal{R} as functions of the 2–10 keV hard continuum flux for our ten time intervals. The iron line flux is in units of 10^{-5} ergs cm^{-2} s^{-1} , and the 2–10 keV hard continuum flux is in units of 10^{-11} ergs s^{-1} cm^{-2} . The dotted curves are the expected relationships in simple reflection models, while the solid curves are the best fits assuming various functional forms (see text). One-sigma error bars are shown.

Since the relative normalization of the Compton reflection continuum \mathcal{R} should be proportional to $W_{K\alpha}$ under a fairly general set of conditions, we would expect that $\mathcal{R} \propto F_{2-10}^{-1}$. Fitting this relationship to the data depicted in Fig. 4c gives $\chi^2/\text{dof} = 14.5/9$ (dotted curve). This is formally inconsistent with the data at the 91% level. Using a more general power-law form $\mathcal{R} \propto F_{2-10}^\alpha$ leads to a vastly improved fit of $\chi^2/\text{dof} = 3.4/8$ with $\alpha = 0.14 \pm 0.60$ (solid curve). This is consistent with a constant relative reflection normalization and implies that $W_{K\alpha}$ and \mathcal{R} do not exhibit the proportionality which is normally expected. In order to examine this explicitly, we plot $W_{K\alpha}$ vs \mathcal{R} in Fig. 5. The dotted line is the linear relationship expected for a cold reflector with solar abundances for which $W_{K\alpha} = 150$ eV when $\mathcal{R} = 1$ (George & Fabian 1991). This model yields a $\chi^2/\text{dof} = 73/10$ and is definitely in conflict with the data. However, if we fit for the proportionality constant, we obtain $W_{K\alpha} = 259$ eV at $\mathcal{R} = 1$ and $\chi^2/\text{dof} = 14.4/9$ which is still formally inconsistent with the data at the 89% level.

6. IMPLICATIONS FOR DISK/CORONA MODELS

If we assume that the *EUVE* light curve is representative of the seed photons for the higher energy X-rays, we can make a simple estimate of the size of the scattering region based upon the delays seen. With each scattering, a seed photon picks up a fractional energy $\Delta E/E \simeq 4k_b T/m_e c^2$, where T is the temperature of the electrons in the corona. The energy of a Comptonized photon will be

$$E \simeq E_0 \left(1 + \frac{4k_b T}{m_e c^2} \right)^n, \quad (2)$$

where E_0 is the initial seed photon energy and n is the number of scatterings (Rybicki & Lightman 1979). The time delay of this photon with respect to the seed photon source will be roughly proportional to the number of scatterings, $t \simeq nt_0$. Here $t_0 \sim l_T/c$ where l_T is the mean free path for Thomson scattering (or the size of the corona if it is optically thin). We take the effective photon energy in the 0.5–1 keV *ASCA* data to be

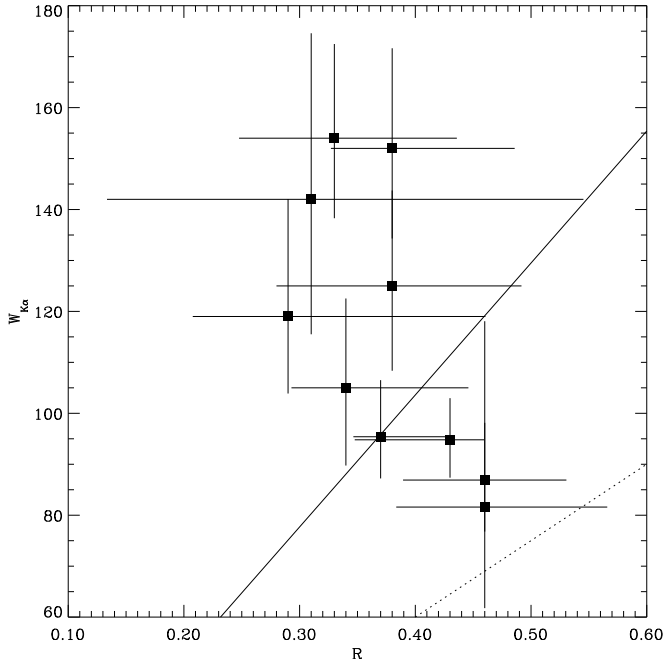


FIG. 5.— Iron line equivalent width $W_{K\alpha}$ versus the relative Compton reflection normalization \mathcal{R} . The dotted line is the expected linear relationship assuming solar abundances for the cold reflector (George & Fabian 1991). The solid line is the best-fit proportionality relationship which is still in conflict with the data at the 89% level.

$E_a = 0.78$ keV and the effective photon energy of the 2–20 keV *RXTE*-PCA data to be $E_{pca} = 5.4$ keV. Both of these energies are determined using the instrument sensitivities in the relevant bands and assuming a photon spectral index of 1.9 and a neutral absorbing column of 1.7×10^{20} cm². Using a value of $k_b T \sim 50$ keV which is found from fits to the *OSSE* spectrum of NGC 5548 (Magdziarz et al. 1998) and the inferred lags of the *RXTE*-PCA and 0.5–1 keV *ASCA*-SIS light curves relative to that of the *EUVE*, we solve for the characteristic time between scatterings and find $t_0 \sim 3.8$ ksec.² For a homogeneous corona with Thomson depth of $\tau \sim 2$ this implies a coronal size scale of $\sim 2 \times 10^{14}$ cm, which is of order $10r_g$ for a $10^8 M_\odot$ black hole.

This interpretation for the relationship between the EUV and higher energy X-ray flux is not without its complications. First of all, as we note above, the fractional size of the step in the EUV is larger than the steps in the higher energy bands. Second, the amplitude of the *EUVE* PSD differs from that of the *RXTE*-PCA (Fig. 3). Therefore a strictly linear relationship between the fluxes in these bands is not possible. One possibility is that the *EUVE* observations are sampling the Wien tail of a black-body spectrum so that the observed variations are more pronounced and are not necessarily characteristic of the bulk of the seed photons. A more provocative explanation would be that the increase in soft photon flux produces excess cooling in the corona, changing some combination of the corona temperature, size, or optical depth. The softening of the underlying continuum with increased flux (Fig. 4a) does in fact show that properties of the corona must be changing.

The iron line fluxes and reflection fractions also have significant implications for the corona/disk geometry. As we noted above, both the reflection fraction and the iron line equivalent width are substantially smaller than has been previously seen

for this object as well as for other type 1 Seyferts (e.g., MCG–6–30–15, Lee et al. 1998; and IC 4329A, Madejski et al. 1995), for which values of $\mathcal{R} \sim 1$ and $W_{K\alpha} \gtrsim 160$ eV are more typical. The lower values we find for NGC 5548 would be consistent with a substantially smaller covering factor for the cold material. This could occur, for example, if the Comptonizing region lay inside an inner disk radius as has been posited for models of Cygnus X-1 (Dove et al. 1997; Gierliński et al. 1997). Alternatively, the disk could extend beneath the corona but may be completely ionized preventing this material from contributing to either the line fluorescence or the reflection hump. Mildly relativistic motion of the Comptonizing medium away from the disk could also account for the lower reflection fractions and iron line equivalent widths (Reynolds & Fabian 1997; Beloborodov 1999).

However, a lack of proportionality between the iron line equivalent width and reflection fraction (Fig. 5) cannot be accounted for simply by the relative geometry of the disk and corona. A constant iron line flux would suggest that a substantial portion of that emission is produced very far from the Comptonizing X-ray source, perhaps in the outer disk or obscuring torus, so that the line emission does not vary on time scales as short as that of the underlying continuum. We would then expect that the reflection hump is likewise produced in this same distant material so that its absolute normalization should also be constant. Unfortunately, there is the additional complication that the Gaussian and diskline fits to the fluorescent iron line indicate that the line is broad and redshifted. The line shapes are consistent with a significant fraction of this emission originating from an accretion disk within $\sim 20r_g$. Furthermore, spectral fits to the *ASCA*-SIS data which include a narrow line at 6.4 keV along with the diskline model yield a narrow component that can contribute only about 15% to the total line flux. Therefore, based on the spectral shapes of the iron line, a significant amount of reprocessing by distant cold material is unlikely.

Wherever the cold reprocessor is located, these results appear to be somewhat in conflict with models in which the spectral variability of the underlying continuum is linked to the relative reflection normalization \mathcal{R} (Magdziarz et al. 1998; Zdziarski et al. 1999). In Fig. 6, we plot the relative Compton reflection normalization versus the photon spectral index of the underlying power-law (filled squares, solid contours). As we note above, these data are formally consistent with a constant value of \mathcal{R} , but there does seem to be a slight linear trend in the same sense predicted by the models. For direct comparison, we also plot in Fig. 6 the spectral parameters found by Zdziarski et al. (1999; see also Magdziarz et al. 1998) which are derived from *Ginga* observations. In this figure, we show the $1\text{-}\sigma$ error contours for both sets of data. The spectral parameters we find appear to occupy a different region of the \mathcal{R} - Γ plane than that found by these previous observations. However, consideration of systematic uncertainties may alter this conclusion. *Ginga*-LAC observations of the Crab have yielded a photon index of $\Gamma = 2.08 \pm 0.03$ (Turner et al. 1989) which agrees with early rocket measurements by Toor & Seward (1974). In contrast, power-law fits to *RXTE*-PCA observations of the Crab yield a significantly softer index of $\Gamma = 2.187$ (Wilms et al. 1999). If this difference of $\Delta\Gamma \sim 0.1$ is due to a systematic shift in measured power-law spectral index, then one may be tempted to shift each of our values of Γ downward by this amount, making

²One can also use the direct lag measured between the *ASCA*-SIS and *RXTE*-PCA light curves of 5 ks. From that lag, one finds $t_0 \sim 0.9$ ks.

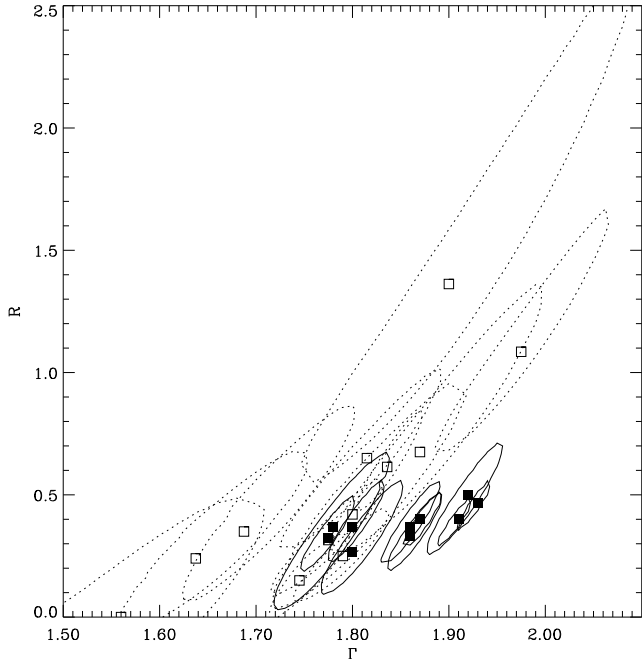


FIG. 6.— The relative Compton reflection normalization \mathcal{R} versus photon spectral index Γ for our fits to the *RXTE*-PCA data (filled squares, solid error contours) and for fits to *Ginga* data as presented in Zdziarski et al. (1999; unfilled squares, dotted contours). Although the *RXTE*-PCA parameters are formally consistent with a constant value of \mathcal{R} , a linear trend may be present. However, the dependence on Γ found for these data is weaker than that found by Zdziarski et al. (1999), and these parameters appear to occupy a different part of the \mathcal{R} - Γ plane. One-sigma contours are shown.

the two sets of parameters consistent. Unfortunately, the orientation of the error contours clearly indicates a correlation between fitted values of \mathcal{R} and Γ . This seems to be an intrinsic feature of the model. If so, any systematic shift of Γ probably also implies a bias in the fitted value of \mathcal{R} as well. It is therefore not entirely clear whether these two datasets can be made consistent even if one considers the possible systematic errors.

As a final caveat, we note that the strength of the reflection component can be masked by features in the hard continuum which need not be well-represented by a power-law. Stern et al. (1995) point out that for Comptonizing regions which are localized and which are illuminated anisotropically the resulting hard continuum will have spectral breaks just above the peak energies of the twice scattered photons (see also Haardt 1993). For sufficiently high values of the compactness ($\equiv L_{\text{diss}}\sigma_T/hm_e c^3$ where L_{diss} is the power heating the corona and h is the coronal size scale), these breaks may occur at energies such that the reflection component will be underestimated. In addition, as the compactness increases, the spectrum will soften and the break will move to lower energies. Hence, any variability in the absolute normalization of the reflection component which is inferred from PEXRAV-type spectral fits could be significantly affected by changes in the compactness. This sort of uncertainty can only be resolved by more sophisticated spectral models.

7. SUMMARY AND CONCLUSIONS

Here we summarize the main results of this work:

1. The EUV leads the harder X-rays, rejecting scenarios in which the soft X-ray component is produced by reprocessing of harder X-rays. In this respect, these hard X-ray lags are reminiscent of the X-ray lags seen in NGC 7469 (Nandra et al. 1998).
2. However, in contrast to NGC 7469, the shorter lags we find for NGC 5548 are consistent with Compton diffusion time scales for a relatively small corona of size $\sim 10^{14}$ cm.
3. The power spectrum of the X-ray variability shows a break at ~ 200 day time scales. The PSD is similar to that seen in NGC 3516; and if one assumes a $10^8 M_\odot$ black hole for NGC 5548, this scales appropriately with mass compared to PSDs seen for the low/hard states of GBHCs such as Cyg X-1 or GX 339-4.
4. The iron line equivalent width and relative reflection normalizations are smaller than those which are typically observed for type 1 Seyferts.
5. The broad, redshifted iron line profiles, the variability of the iron line equivalent width, and the apparent constancy of the relative reflection normalization are difficult to reconcile in the context of simple reflection models.

The last point, while not definitively constrained by the data, may pose a serious challenge for models of reflection by cold material and will only be resolvable with further detailed temporal and spectral observations. More sensitive studies with future instruments such as *XMM* would be extremely useful to verify this result.

We would like to thank Andrzej Zdziarski for useful conversations. JC, MAN, and NM thank the Program on Black Hole Astrophysics at the Institute for Theoretical Physics (ITP) at the University of California, Santa Barbara for hosting them during part of this effort. The ITP is supported by NSF Grant PHY 94-07194. JC was supported by the NASA/ADP grant NAG5-7897 and the NASA/RXTE grant DPR S-92675F. Part of this work was performed while JC held a National Research Council-NRL Research Associateship. CSR thanks support from NASA under LTSA grant NAG5-6337 and support from Hubble Fellowship grant HF-01113.01-98A awarded by the Space Telescope Institute, which is operated by the Association of Universities for Research in Astronomy, Inc., for NASA under contract NAS 5-26555. OB was supported by NASA/RXTE grant NAG5-7125. We would like to thank the *RXTE* Guest Observer Facility for help with the data analysis and Tod Strohmeyer for providing software for constructing the PCA collimator model. In conducting this research, we have made extensive use of the NASA Astrophysics Data System (ADS) Abstract and Article services. We acknowledge use of the ADS Digital Library; the NASA/IPAC Extragalactic Database (NED) which is operated by the Jet Propulsion Laboratory, Caltech, under contract with NASA; and the HEASARC data archive.

REFERENCES

- Alexander, T. 1997, in *Astronomical Time Series*, ed. D. Maoz et al. (Netherlands: Kluwer Academic Publishers), 163
- Belloni, T., & Hasinger, G. 1990a, *A&A*, 227, L33
- Beloborodov, A. M. 1999, *MNRAS*, 305, 181
- Clavel, J., et al. 1991, *ApJ*, 366, 64
- Clavel, J., et al. 1992, *ApJ*, 393, 113
- Courvoisier, T. J.-L., & Clavel, J. 1991, *A&A*, 248, 389
- Czerny, B., Schwarzenberg-Czerny, A., & Loska, Z. 1999, *MNRAS*, 303, 148
- Dove, J. B., Wilms, J., Maisack, M., & Begelman, M. C. 1997, *ApJ*, 487, 759
- Edelson, R. A., & Krolik, J. H. 1988, *ApJ*, 333, 646
- Edelson, R., & Nandra, K., 1999, *ApJ*, 514, 682
- Fabian, A., Rees, M. J., Stella, L., & White, N. E. 1989, *MNRAS*, 238, 729
- George, I. M., & Fabian, A. 1991, *MNRAS*, 249, 352
- Gierliński, M., et al. 1997, *MNRAS*, 288, 958
- Glasser, C. A., Odell, C. E., & Seufert, S. E. 1994, *IEEE Trans. Nucl. Sci.*, NS-41, 4
- Haardt, F. 1993, *ApJ*, 413, 680
- Horne, J.H., & Bailunas, S.L., 1986, *ApJ*, 302, 757
- Kaastra, J. S., & Barr, P. 1989, *A&A*, 226, 59
- Koratkar, A., & Blaes, O. 1999, *PASP*, 111, 1
- Korista, K. T., et al. 1995, *ApJS*, 97, 285
- Lee, J., et al. 1998, *MNRAS*, 300, 583
- Levine, A. M., Bradt, H., Cui, W., Jernigan, J. G., Morgan, E. H., Remillard, R., Shirey, R. E., & Smith, D. A., 1996, *ApJ*, 469, L33
- Lochner, J., & Remillard, R., 1997, *ASM Data Products Guide*, Version Dated August 27, 1997, http://heasarc.gsfc.nasa.gov/docs/xte/asm_products_guide.html
- Lomb, N. R., 1976, *Ap&SS*, 39, 447
- Madejski, G. M., et al. 1995, *ApJ*, 438, 672
- Magdziarz, P., & Zdziarski, A. A. 1995, *MNRAS*, 273, 837
- Magdziarz, P., et al. 1998, *MNRAS*, 301, 179
- Malkan, M. A. 1991, in *Structure and Properties of Accretion Disks*, ed. C. Bertout et al. (Paris: Éditions Frontières), 165
- Marshall, H. L., et al. 1997, *ApJ*, 479, 222
- Marshall, F. E., et al. 1998, *Nucl. Phys. B. (Proc. Suppl.)*, 69/1-3, 640
- Miyamoto, S., & Kitamoto, S., 1989, *Nature*, 342, 773
- Miyamoto, S., Kitamoto, S., Iga, S., Negoro, H., & Terada, K., 1992, *ApJ*, 391, L21
- Nandra, K., et al. 1991, *MNRAS*, 248, 760
- Nandra, K., et al. 1993, *MNRAS*, 260, 504
- Nandra, K., et al. 1998, *ApJ*, 505, 594
- Nowak, M. A., Vaughan, B. A., Wilms, J., Dove, J., & Begelman, M. C., 1999a, *ApJ*, 510, 874
- Nowak, M. A., Wilms, J., & Dove, J. B., 1999b, *ApJ*, 517, in press
- Remillard, R. A., & Levine, A. M., 1997, in *All-Sky X-Ray Observations in the Next Decade*, ed. N. Matsuoka, N. Kawai, (Tokyo: Riken), 29
- Reynolds, C. S., & Fabian, A. C. 1997, *MNRAS*, 290, L1
- Peterson, B. M., et al. 1991, *ApJ*, 368, 119
- Press, W. H., Teukolsky, S. A., Vetterling, W. T., & Flannery, B. P. 1992, *Numerical Recipes* (New York: Cambridge University Press), p. 636
- Rybicki, G. B., & Lightman, A. P. 1979, *Radiative Processes in Astrophysics* (New York: Wiley-Interscience), p. 208
- Scargle, J. D., 1982, *ApJ*, 263, 835
- Scargle, J. D. 1989, *ApJ*, 343, 874
- Stern, B. L., Poutanen, J., Svensson, R., Sikora, M., & Begelman, M. C. 1995, *ApJ*, 449, L13
- Toor, A., & Seward, F. D. 1974, *AJ*, 79, 995
- Turner, M. J. L., et al. 1989, *PASJ*, 41, 345
- Vaughan, B.A., & Nowak, M.A., 1997, *ApJ*, 474, L43
- Wilms, J., et al. 1999, *ApJ*, in press
- Zdziarski, A. A., Lubinski, P., & Smith, D. A. 1999, *MNRAS*, 303, L11

Obs.	Date	Exp. time (ks)	mean count rate (10^{-2} cps)	Spectral Density at 76\AA (μJy)
	02 Jun	8.8	18.0 ± 0.6	345
	09 Jun	11.5	8.4 ± 0.4	161
2	18 Jun	139.8	9.3 ± 0.1	178
3	01 Jul	21.3	2.1 ± 0.2	40

TABLE 1
EUVE-DS OBSERVATIONS

Obs.	Date	good SIS exp. time (ks)	good GIS exp. time (ks)	SIS0 count rate (cps)	GIS2 count rate (cps)	2–10 keV flux (10^{-11} erg cm^{-2} s^{-1})
1	15 Jun 1998	21.2	25.3	2.61	1.56	5.9
2	20 Jun 1998	111.1	106.3	3.07	1.71	6.9
3	01 Jul 1998	9.2	10.6	1.66	0.97	4.2
4	07 Jul 1998	14.7	16.9	1.73	1.08	4.3
	19 Jan 1999	8.2	9.0	1.84	1.09	4.7

TABLE 2

BASIC PARAMETERS OF OUR ASCA OBSERVATIONS OF NGC 5548. THE QUOTED FLUXES ARE THOSE OBSERVED (I.E. SUBJECT TO THE TOTAL LINE-OF-SIGHT ABSORPTION). A SIMPLE POWER-LAW MODEL WAS USED TO MEASURE THESE FLUXES.

Obs.	Date(s)	target	Good Time (ks)	PCA/PCUs 0–2 rate (cps)	HEXTE rate (cps)
1	Jun 15–16	NGC 5548	21.24	25.9	1.0
		1E 1415.6+2557	8.82	4.8	...
2	Jun 19–24	NGC 5548	110.28	28.7	0.7
		1E 1415.6+2557	7.56	4.4	...
		NGC 5548 scan	3.48
3	Jun 29–Jul 2	NGC 5548	41.70	19.3	0.6
		1E 1415.6+2557	7.44	5.2	...
4	Jul 7	NGC 5548	24.60	19.3	1.0
		1E 1415.6+2557	3.60	4.2	...
		Aug 16–18	NGC 5548	44.92	23.8
		1E 1415.6+2557	7.74	7.3	...

TABLE 3
RXTE OBSERVATIONS

Instruments	t_{lag} (ks)	99.9% C.L. (ks)	
EUVE vs ASCA	13.1	–3.9	29.5
EUVE vs RXTE PCA	35.3	23.1	53.1
ASCA vs RXTE PCA	5.0	1.9	8.0

TABLE 4

LAGS OBTAINED USING THE ZDCF FOR THE THREE PAIR-WISE COMBINATIONS OF INSTRUMENTS DURING THE 18–23 JUNE 1998 OBSERVATION PERIOD.

Obs.	PCA/PCUs 0–2 rate (cps)	Γ	A (10^{-3})
1	4.8 ± 0.2	2.3 ± 0.1	$9.8(-1.3/+3.8)$
2a	3.9 ± 0.3	2.4 ± 0.2	$11.6(-2.8/+3.8)$
2b	4.8 ± 0.3	2.2 ± 0.2	$8.8(-2.1/+2.8)$
3a	5.4 ± 0.2	2.3 ± 0.1	$11.1(-2.0/+2.4)$
3b	4.9 ± 0.2	2.2 ± 0.1	$9.3(-1.6/+2.0)$
4	4.2 ± 0.3	2.3 ± 0.1	$11.6(-2.3/+2.9)$
Aug 16–18	7.3 ± 0.2	2.1 ± 0.1	$10.8(-1.0/+1.0)$

TABLE 5
PROPERTIES OF 1E 1415.6+2557.

Obs.	F_{2-10}	Γ		\mathcal{R}	GAUSSIAN		N_i	χ^2/dof
		SIS	PCA		E (keV)	σ (keV)		
1	8.0	...	1.86 ± 0.03	$0.34^{+0.18}_{-0.08}$	$6.15^{+0.10}_{-0.11}$	< 0.41	$8.1^{+2.3}_{-2.0}$	47.4/40
	7.9	1.89 ± 0.03	$1.86^{+0.03}_{-0.01}$	$0.40^{+0.20}_{-0.07}$	$6.15^{+0.13}_{-0.12}$	$0.35^{+0.17}_{-0.11}$	$7.0^{+1.7}_{-1.5}$	382/381
2.1	7.8	...	1.86 ± 0.03	$0.38^{+0.19}_{-0.17}$	$6.15^{+0.11}_{-0.12}$	$0.33^{+0.16}_{-0.18}$	$10.6^{+2.7}_{-2.4}$	38.4/40
	7.7	$1.88^{+0.05}_{-0.04}$	1.86 ± 0.03	$0.40^{+0.19}_{-0.18}$	$6.17^{+0.10}_{-0.11}$	$0.30^{+0.18}_{-0.15}$	$8.1^{+1.9}_{-1.7}$	327/324
2.2	9.8	...	1.93 ± 0.02	0.46 ± 0.12	6.10 ± 0.12	$0.44^{+0.13}_{-0.12}$	$9.1^{+2.0}_{-1.8}$	36.0/40
	9.7	$1.94^{+0.03}_{-0.02}$	1.91 ± 0.02	$0.41^{+0.16}_{-0.10}$	6.11 ± 0.12	$0.35^{+0.26}_{-0.09}$	$6.5^{+2.5}_{-0.9}$	501/409
2.3	9.5	...	$1.90^{+0.02}_{-0.01}$	$0.37^{+0.10}_{-0.04}$	$6.18^{+0.13}_{-0.07}$	$0.35^{+0.15}_{-0.11}$	$9.6^{+1.9}_{-1.4}$	29.8/40
	9.4	1.93 ± 0.02	$1.90^{+0.02}_{-0.03}$	$0.40^{+0.14}_{-0.05}$	$6.17^{+0.15}_{-0.06}$	$0.41^{+0.12}_{-0.10}$	8.1 ± 1.3	423/416
2.4	9.1	...	$1.91^{+0.04}_{-0.03}$	$0.46^{+0.18}_{-0.13}$	$6.32^{+0.22}_{-0.29}$	< 0.74	$7.5^{+5.7}_{-3.1}$	32.2/40
	8.8	$1.95^{+0.06}_{-0.04}$	$1.91^{+0.05}_{-0.03}$	$0.49^{+0.30}_{-0.12}$	$6.25^{+0.25}_{-0.20}$	$0.46^{+0.30}_{-0.23}$	$6.2^{+3.4}_{-1.9}$	241/286
Jun 29	6.9	...	$1.80^{+0.05}_{-0.04}$	$0.29^{+0.29}_{-0.14}$	6.21 ± 0.12	< 0.36	$8.8^{+2.9}_{-1.9}$	26.0/40
3	5.6	...	$1.80^{+0.03}_{-0.02}$	$0.38^{+0.18}_{-0.09}$	$6.20^{+0.09}_{-0.82}$	$0.38^{+0.14}_{-0.13}$	$9.1^{+2.0}_{-1.8}$	28.0/40
	5.3	$1.78^{+0.06}_{-0.04}$	$1.82^{+0.04}_{-0.02}$	$0.62^{+0.33}_{-0.13}$	6.16 ± 0.14	$0.44^{+0.17}_{-0.11}$	7.3 ± 1.4	202/278
Jul 2	5.4	...	1.80 ± 0.04	$0.31^{+0.40}_{-0.30}$	$6.21^{+0.18}_{-0.14}$	< 1.11	$8.2^{+3.2}_{-2.6}$	26.3/40
	5.8	...	1.77 ± 0.03	$0.33^{+0.18}_{-0.14}$	$6.17^{+0.09}_{-0.10}$	$0.39^{+0.12}_{-0.10}$	$9.8^{+2.0}_{-1.7}$	47.0/40
4	5.7	$1.77^{+0.05}_{-0.01}$	$1.75^{+0.03}_{-0.01}$	$0.32^{+0.20}_{-0.07}$	$6.20^{+0.07}_{-0.10}$	$0.29^{+0.14}_{-0.12}$	$7.0^{+0.9}_{-1.0}$	287/332
	Aug 16–18	7.2	...	$1.88^{+0.01}_{-0.02}$	$0.43^{+0.05}_{-0.14}$	$6.08^{+0.11}_{-0.04}$	< 0.17	$7.5^{+1.1}_{-1.0}$

Obs.	F_{2-10}	Γ		\mathcal{R}	DISKLINE		N_i	χ^2/dof
		SIS	PCA		r_{in}	i (deg)		
1	7.9	1.89 ± 0.03	1.86 ± 0.03	$0.39^{+0.19}_{-0.18}$	$9.5^{+7.2}_{-3.5}$	< 32	$6.8^{+1.9}_{-1.5}$	383/381
2.1	7.7	1.88 ± 0.04	1.85 ± 0.03	$0.39^{+0.19}_{-0.17}$	$10.3^{+6.2}_{-3.5}$	< 28	$8.3^{+1.8}_{-1.7}$	327/324
2.2	9.6	1.95 ± 0.02	1.91 ± 0.02	$0.42^{+0.10}_{-0.12}$	$7.6^{+3.7}_{-1.6}$	< 29	$6.8^{+1.5}_{-1.4}$	503/409
2.3	9.4	1.93 ± 0.02	1.90 ± 0.02	$0.38^{+0.12}_{-0.11}$	$8.9^{+6.7}_{-2.9}$	$26^{+6.6}_{-8.2}$	$8.1^{+1.6}_{-1.5}$	420/416
2.4	8.8	1.96 ± 0.05	1.91 ± 0.04	$0.50^{+0.28}_{-0.23}$	$12.1^{+7.7}_{-6.1}$	41^{+18}_{-20}	$6.1^{+2.0}_{-2.3}$	242/286
3	5.4	$1.78^{+0.06}_{-0.04}$	$1.82^{+0.03}_{-0.04}$	$0.59^{+0.27}_{-0.25}$	< 16.4	< 37	$7.3^{+1.6}_{-1.7}$	203/278
4	5.7	1.77 ± 0.04	1.75 ± 0.03	$0.32^{+0.18}_{-0.16}$	$11.3^{+7.0}_{-3.3}$	< 25	$6.9^{+1.6}_{-1.3}$	288/332

TABLE 6

THE PARAMETERS OBTAINED FROM SPECTRAL FITS TO THE *RXTE* AND *ASCA* DATA. THE SPECTRAL MODELS CONSIST OF GALACTIC ABSORPTION, A FLUORESCENT IRON EMISSION LINE, AN UNDERLYING CUT-OFF POWER-LAW AND A COMPTON REFLECTION COMPONENT. FOR FITS IN THE UPPER PART OF THE TABLE, A BROAD GAUSSIAN FUNCTION IS USED TO MODEL THE IRON LINE; IN THE LOWER PART, A DISKLINE MODEL IS USED. FOR THE JOINT *ASCA-SIS/RXTE-PCA* FITS, WE REPORT SEPARATE SPECTRAL INDICES FOR THE UNDERLYING POWER-LAW FOR SIS AND PCA. THE 2–10 KEV CONTINUUM FLUX IS REPORTED FOR THE PCA FITS ONLY AND IS IN UNITS OF 10^{-11} ERGS $\text{CM}^{-2}\text{S}^{-1}$. THE IRON LINE FLUX, N_i , IS IN UNITS OF 10^{-5} ERGS $\text{CM}^{-2}\text{S}^{-1}$, AND THE INNER RADIUS OF THE DISKLINE MODEL, r_{in} IS IN UNITS OF $r_g = GM/c^2$.